



Boosting photocatalytic hydrogen evolution: Orbital redistribution of ultrathin ZnIn_2S_4 nanosheets via atomic defects

Qingjie Luan^{a,b,1}, Xiangdong Xue^{a,1}, Rongjie Li^a, Lin Gu^c, Wenjun Dong^{a,b,*}, Dongxue Zhou^{a,b}, Xing Wang^{a,b}, Baozhen Li^{a,b}, Ge Wang^{a,**}, Changmin Hou^d

^a Beijing Advanced Innovation Center for Materials Genome Engineering, Beijing Key Laboratory of Function Materials for Molecule & Structure Construction, School of Materials Science and Engineering, University of Science and Technology Beijing, Beijing 100083, PR China

^b Shunde Graduate School of University of Science and Technology Beijing, Foshan 528399, PR China

^c Beijing Laboratory for Electron Microscopy Institute of Physics, Chinese Academy of Sciences Beijing, 100190, PR China

^d State Key Laboratory of Inorganic Synthesis & Preparative Chemistry, College of Chemistry, Jilin University, Changchun 130012, PR China

ARTICLE INFO

Keywords:

In vacancies

ZnIn_2S_4

Photocatalyst

Hole regulation

Orbital redistribution

ABSTRACT

Defect engineering, inducing photo-excited electrons and holes to different surfaces of semiconductor photocatalyst, is an efficient strategy to improve the photocatalytic activity. A rapid heating-up hydrothermal technique is developed to regulate ZnIn_2S_4 crystal growth, then, ultrathin ZnIn_2S_4 nanosheets with In defect-rich $[\text{InS}]_6$ interlayer but perfect $[\text{InS}]_4$ and $[\text{ZnS}]_4$ surface layers are successfully prepared (ultra-ZIS- V_{In}). Interestingly, the In defect, inducing the redistribution of the orbitals near the valence band maximum, separates the oxidation and reduction sites on the opposite sides of the ultra-ZIS- V_{In} nanosheets. Simultaneously, In defects increase the density of states (near the valence band maximum and conduction band minimum) and delocalize the electron around In defects. Accordingly, the photocatalytic hydrogen evolution rate is optimized to $13.4 \text{ mmol h}^{-1} \text{ g}^{-1}$, which is 8.9 times higher than that of defect-free ZnIn_2S_4 (pristine-ZIS).

1. Introduction

Hydrogen (H_2), as an effective, secure, and sustainable energy source, is an ideal candidate to solve energy and environmental crisis [1–4]. Up to now, various technologies, such as coal gasification, high temperature pyrolysis of water, and photo-electrocatalytic water splitting, have been developed to produce hydrogen energy [5,6]. Especially, photocatalytic hydrogen production, as a promising technology for environmental protection, simple operation, and wide application, can convert solar energy into renewable hydrogen [7–9]. Therefore, exploring high-performance photocatalysts that can regulate photo-generated carriers' generation, separation/migration, and consumption, is a crucial issue in photocatalytic hydrogen evolution. However, randomly in-plane carriers migration leads to the rapid recombination of photo-induced electrons and holes, which severely inhibits the photocatalytic activity [10,11]. Hence, designing advanced photocatalysts that can enhance the spatial-directed separation and

migration of photogenerated carriers is highly desired [12–14].

The layered ZnIn_2S_4 is an excellent candidate for photocatalyst, owing to its high activity, favorable chemical stability and appropriate band gap [15,16]. Up to now, various strategies, such as doping, heterostructure and defects engineering, have been developed to improve its photocatalytic activity [17–19]. Firstly, doping ions into semiconductor introduces the donor/acceptor level, which can regulate the concentration and energy distribution of the carriers near the conduction/valence band edge, and then improve the electron transition behavior. For example, cation-doping (such as Cu or Ni doped in ZnIn_2S_4) results in that Fermi level passes through conduction band. It endows the material with metallic properties, leading to the enhancement of electrical conductivity and photo-generated carriers migration ability [20,21]. Anion-doping (such as N or O doped ZnIn_2S_4) can regulate valence band to promote the mobility of holes, and elevate conduction band to enhance the reducibility of photo-generated electrons [10,22]. Secondly, effective interfacial electric field in

* Corresponding author at: Beijing Advanced Innovation Center for Materials Genome Engineering, Beijing Key Laboratory of Function Materials for Molecule & Structure Construction, School of Materials Science and Engineering, University of Science and Technology Beijing, Beijing 100083, PR China.

** Corresponding author.

E-mail addresses: wdong@ustb.edu.cn (W. Dong), gewang@mater.ustb.edu.cn (G. Wang).

¹ These authors contributed equally to this work.

heterojunction (such as MoS_2 or MoSe_2 anchored on ZnIn_2S_4) prevents the random transmission of photogenerated carriers, facilitating the efficient separation of photogenerated electron-hole pairs [23,24]. Finally, surface defects can directionally capture photogenerated electrons, and then regulate their spatial distribution and extend their lifetime. For instance, surface anion defects (S defects) act as electron traps, capturing photogenerated electrons to suppress the recombination of electrons and holes [8]. Surface cation defects (Zn defects) shunt partial electrons from $[\text{InS}]_4$ to $[\text{ZnS}]_4$ surface layer, realizing the efficient utilization of photogenerated electrons [25]. The interfacial Mo-S bond and internal electric field in $\text{S}_v\text{-ZIS}/\text{MoSe}_2$ photocatalyst achieves Z-scheme charge transfer, significantly promoting the photocatalytic performance [26].

In the sandwich-like ZnIn_2S_4 staking structures, the exposed Zn or S atom on the surface is easily escaped, then Zn or S defect is formed. However, the removal of In atoms located in the interlayer of the sandwich structure is difficult for the steric hindrance, so the interlayered In defects are hard to be created. The Zn defect or S defect, prompts the photogenerated electrons directed migration, but almost no effect on the hole regulation. Due to the periodic electrostatic potential endowed by the S-Zn-S-In-S-In-S staking structures of ZnIn_2S_4 , the migration of photogenerated holes to the surface of ZnIn_2S_4 is blocked, which inhibits the oxidative half-reaction [22,23,27]. In order to transport photogenerated electrons and holes to the surface simultaneously, ultrathin ZnIn_2S_4 nanosheets with interlayer In vacancies were prepared by a rapid heating-up hydrothermal process. The In vacancies disturb the periodic potential field of ZnIn_2S_4 , and then the orbitals near the valence band maximum (VBM) distributed in the interlayer originally were redistributed on the $[\text{ZnS}]_4$ surface layer. Meanwhile, orbitals near the conduction band minimum (CBM) still stay around the $[\text{InS}]_4$ surface layer. Hence, the reduction and oxidation sites are redistributed on the opposite sides of ultra-ZIS- V_{In} nanosheets, which achieves the efficient utilization of photogenerated electrons and holes. In addition, the enhanced density of states (DOS) near the VBM and CBM confirms that more electrons could participate in the photocatalytic reaction. Ultra-ZIS- V_{In} nanosheet with efficient charge separation and enhanced DOS exhibits superior photocatalytic performance. The photocatalytic hydrogen reaction rate can reach up to $13.4 \text{ mmol h}^{-1} \text{ g}^{-1}$ under visible light irradiation, which is 8.9-fold compared with that of pristine-ZIS ($1.5 \text{ mmol h}^{-1} \text{ g}^{-1}$).

2. Experimental section

2.1. Chemical

Indium chloride tetrahydrate ($\text{InCl}_3 \cdot 4\text{H}_2\text{O}$) and triethanolamine (TEOA) were obtained from Aladdin. Zinc acetate dehydrate (Zn (CH_3COO) $_2 \cdot 2\text{H}_2\text{O}$) and thioacetamide (TAA) were purchased from Alfa Aesar. All the chemicals were analytical reagent (AR) grade, obtained from commercial sources without further purification. Deionized water ($18.2 \text{ M}\Omega \text{ cm}^{-1}$) was used in all the experiments.

2.2. Materials preparation

2.2.1. Synthesis of pristine ZnIn_2S_4 nanosheets

The synthesis process of the pristine ZnIn_2S_4 is similar to the solvothermal route in reported literature with some modifications [25]. Typically, 0.8 mmol (0.175 g) Zn (CH_3COO) $_2 \cdot 2\text{H}_2\text{O}$, 1.6 mmol (0.469 g) $\text{InCl}_3 \cdot 4\text{H}_2\text{O}$, 6.4 mmol (0.481 g) TAA are dissolved in 30 mL H_2O and 30 mL ethanol with ultrasonic dispersion 10 min, and then vigorous stirring for 30 min in room temperature. After that, the mixture solution is poured into a Teflon vessel held in a stainless-steel autoclave sealed (100 mL in capability), and heated at 200°C for 24 h with a heating-up rate of $2^\circ\text{C}/\text{min}$. After cooling to room temperature naturally, the obtained yellow precipitate is collected by centrifugation, washed by water and ethanol for several times. Finally, the washed precipitate is dried in

the vacuum freeze-drying equipment for two days. The obtained yellow powder is denoted as pristine-ZIS.

2.2.2. Synthesis of ultrathin ZnIn_2S_4 nanosheets with In vacancies

The synthetic method is similar with the synthesis process of the pristine-ZIS. Differently, the sealed Teflon vessel held in a stainless-steel autoclave is heated to 200°C for 24 h with different heating-up rate. A series of ultra-ZIS- V_{In} with heating-up rate $2.5^\circ\text{C}/\text{min}$, $5^\circ\text{C}/\text{min}$, $7.5^\circ\text{C}/\text{min}$, $10^\circ\text{C}/\text{min}$ are prepared, which are classified as ultra-ZIS- $\text{V}_{\text{In}}-2.5$, ultra-ZIS- $\text{V}_{\text{In}}-5$, ultra-ZIS- $\text{V}_{\text{In}}-7.5$, ultra-ZIS- $\text{V}_{\text{In}}-10$.

2.2.3. Deposition of metal (Ag) and metal oxides (Co_3O_4)

For the photo-deposition experiments, 0.10 g ZnIn_2S_4 photocatalysts are dispersed into 100 mL of deionized water. After the addition of a certain amount of AgNO_3 (1 wt% of photocatalysts), the suspension is irradiated by a 300 W Xe lamp for 30 min under continuous stirring. Ag-loaded photocatalysts are collected by centrifugation after the photocatalytic reactions. Photo-deposition of Co_3O_4 is carried out by a similar method, using $\text{Co}(\text{NO}_3)_2$ as precursor.

2.3. Characterization

The crystalline structure and phase are characterized by powder X-ray diffraction (XRD, Bruker D8-Advance) with Cu K α radiation (40 kV, 40 Ma, $\lambda = 1.5406 \text{ \AA}$). The XRD pattern is recorded from 10° to 80° (2θ) with a scanning step of 5 min^{-1} . The morphologies and microstructure are characterized by scanning electron microscope (SEM, Hitachi SU 8010). HRTEM and elemental mapping are recorded with a JEM-2200FS. The HAADF-STEM images are obtained from a JEOL JEM-ARM200F TEM/STEM with a spherical aberration corrector. Determination of the elements content has been determined taken by means of ICP-OES (Agilent, ICP-OES 730). XPS data is recorded via an ESCALAB 250 Xi system (Thermo Electron Corporation). The room-temperature electron spin resonance spectra (ESR), recorded on a Bruker A300 EPR spectrometer at 300 K and 9.86 GHz, proves the existence of In defects in ultra-ZIS- V_{In} nanosheets. The FluorMAX-4 spectrophotometer is applied to get PL spectra. The time-resolved photoluminescence spectroscopy is characterized by an FLS 980 fluorescence spectrometer with excitation at 475 nm. UV-vis diffuse reflectance spectra (UV-vis DRS) is recorded at the range from 300 to 800 nm by a Shimadzu UV-2550, and BaSO_4 was applied as a reflectance standard. The femtosecond pump-probe transient absorption spectroscopy (TA) analysis is recorded on a femtosecond pump-probe spectrometer (NanoLOG-TCSPC) coupled to an ultrafast amplified laser system. The 400 nm pump pulses are from an optical parametric amplifier excited. The white-light continuum probe (450–680 nm) is generated by focusing a small portion of the 800 nm beam onto a rotating CaF_2 plate (thickness $\sim 5 \text{ mm}$). The instrument response function is estimated to be $\sim 100 \text{ fs}$ by a routine optical cross-correlation procedure. All electrochemical and photoelectrochemical measurements are conducted on CHI-660D electrochemical workstation with a three-electrode system. In the typical three-electrode system, the working electrode is the fluoride tin oxide (FTO) with the as-prepared photocatalyst, the reference electrode is standard calomel electrode (SCE), and the counter electrode was graphite sheet. Electrochemical measurements are carried out in Na_2SO_4 (0.5 M, pH = 6.8) solution. The electrochemical impedance spectroscopy (EIS) is conducted under open-circuit potential with $0.01\text{--}1 \times 10^4 \text{ Hz}$ frequency range and 0.005 V amplitude. The photocurrent response is tested under 300 Xe lamp. Transient photocurrent measurements with chopped illumination are also conducted under visible-light irradiation (the interval is 40 s for light on and off) at a fixed potential of 0.2 V (vs standard calomel electrode) for 520 s. Mott-Schottky (M-S) plots are collected from -1.5 to 0 V under 10 kHz frequency and 0.01 V amplitude. The Mott-Schottky measurement evaluates the charge carrier density (N_d) based on the following equation:

Table 1Atomic bond order analysis for ZnIn_2S_4 .

Bond	Order	Spin	Length (Å)
S(III)—In(II)	0.44	-0.02	2.48656
S(IV)—In(II)	1.25	-0.12	2.55599
S(II)—Zn	0.34	-0.02	2.36782
S(I)—Zn	1.48	-0.04	2.37372
S(III)—In(I)	0.57	-0.13	2.78695
S(II)—In(I)	0.75	-0.15	2.71218

$$\frac{1}{C^2} = \left(\frac{2}{e\epsilon\epsilon_0} \right) (V_A - V_{FB} - \frac{kT}{e})$$

$$N_d = \frac{2}{e\epsilon\epsilon_0} \left[\frac{d(1/C^2)}{dV} \right]^{-1}$$

where C, V_A , V_{FB} , k and T are the capacitance at the semiconductor/electrolyte interface (F cm^{-2}), the applied voltage, the flat band potential, the Boltzmann constant and the absolute temperature, respectively. e is the electronic charge (1.602×10^{-19} C), ϵ_0 is the permittivity

of vacuum ($8.854 \times 10^{-14} \text{ F m}^{-1}$), ϵ is the dielectric constant of ZnIn_2S_4 , N_d is the donor density. XAFS spectra at S K-edge are performed at 4B7A beamline of Beijing Synchrotron Radiation Facility (BSRF), China. 4B7A beamline is equipped with a Si (111) double crystal monochromator which is detuned to eliminate higher harmonics. XAFS spectra at Zn K-edge were performed at 4B9A beamline of Beijing Synchrotron Radiation Facility (BSRF), China. XAFS measurements at In K-edge are conducted at the beamline (BL14W1) of Shanghai National Synchrotron Radiation Facility (SSRF, China). The EXAFS data are disposed according to the standard procedures through the ATHENA module implemented in the IFEFFIT software packages. The k^3 -weighted $\chi(k)$ data in the k-space ranging from 3 to 13.5 \AA^{-1} are Fourier transformed to real (R) space using a hanging window ($dk = 1.0 \text{ \AA}^{-1}$) to separate the EXAFS contributions from different coordination shells. To obtain the detailed structural parameters around the In centers in the as-prepared samples, the quantitative curve-fittings are carried out for the Fourier transformed $k^3 \chi(k)$ in the R-space using the ARTEMIS module of IFEFFIT4. Effective backscattering amplitudes $F(k)$ and phase shifts $\Phi(k)$ of all fitting paths are calculated by the ab initio code FEFF6.0. In order to fit the curves in the R-range of $1-4 \text{ \AA}^{-1}$, we consider In-S, and In-In paths as

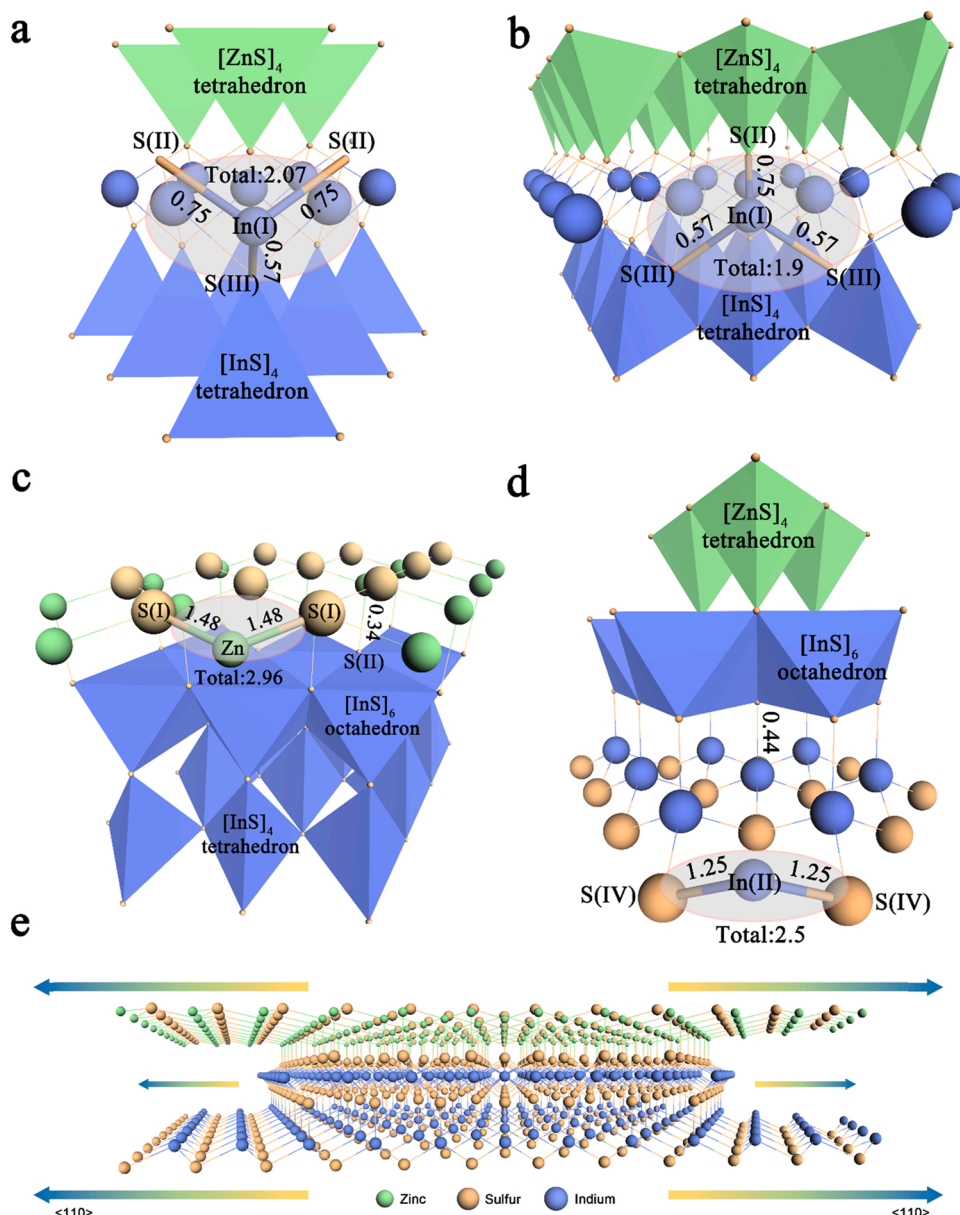


Fig. 1. Partial coordination environment for two configurations of In(I) atoms (a–b), Zn atoms (c), In(II) atoms (d) and the schematic illustration of the growth trend for ZnIn_2S_4 crystal (e). In ZnIn_2S_4 crystal growth process, the Zn atoms coordinate primarily with two S(I) atoms to form two Zn—S(I) bonds (corresponding bond order values of 1.48). While Zn and S(II) bonding unfavorably due to smaller Zn—S(II) bond order (corresponding bond order values of 0.34). Similarly, In(II) atoms coordinate with two S(IV) atoms, forming two In(II)—S(IV) bonds (corresponding bond order values of 1.25) without In—S(III) (corresponding bond order values of 0.44) bond. The In(I) atoms show two possible configurations: one In(I)—S(II) and two In(I)—S(III) bonds (corresponding bond order values of 1.9) or two In(I)—S(II) and one In(I)—S(III) bonds (corresponding bond order values of 2.07), respectively.

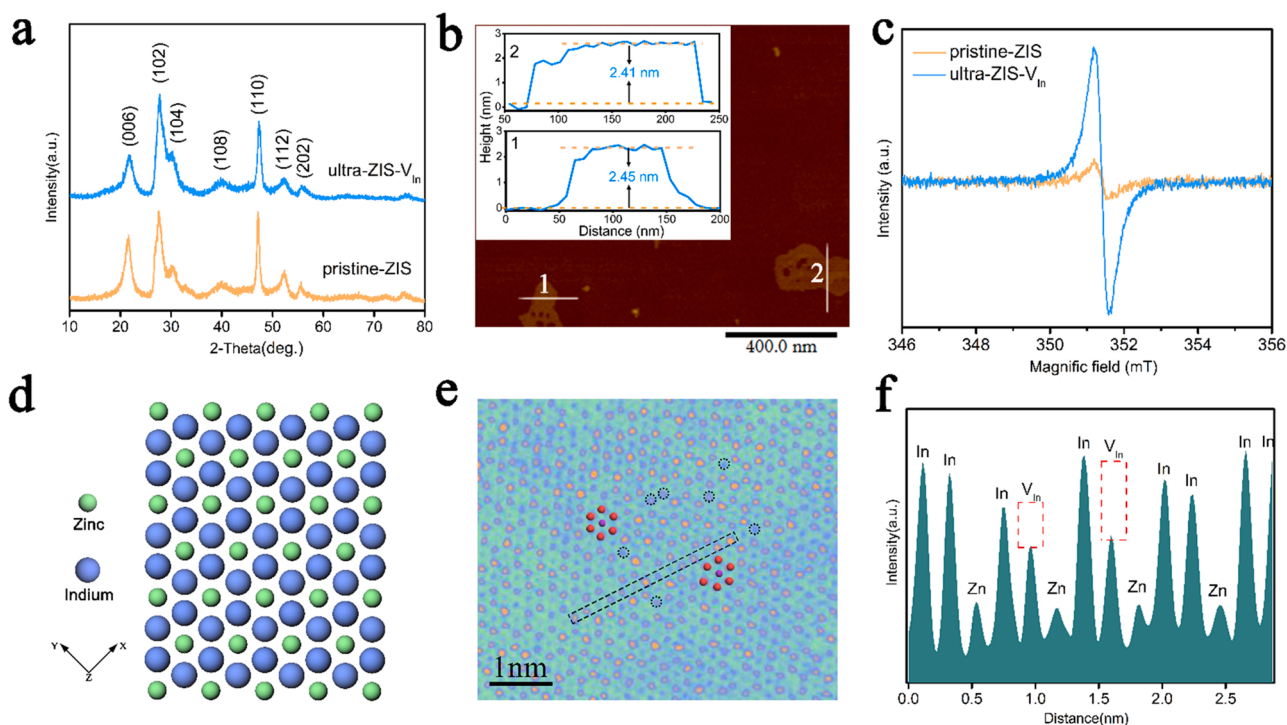


Fig. 2. (a) X-ray diffraction spectra for pristine-ZIS and ultra-ZIS-V_{In}, (b) AFM image (inset is the height profiles of lines 1 and 2) for ultra-ZIS-V_{In} and (c) EPR spectra for pristine-ZIS and ultra-ZIS-V_{In}, and (d) the atomic configuration of (001) plane in ZnIn₂S₄ crystal, (e) HAADF-SATEM images and (f) intensity profile corresponding to the rectangle in (e) for ultra-ZIS-V_{In}.

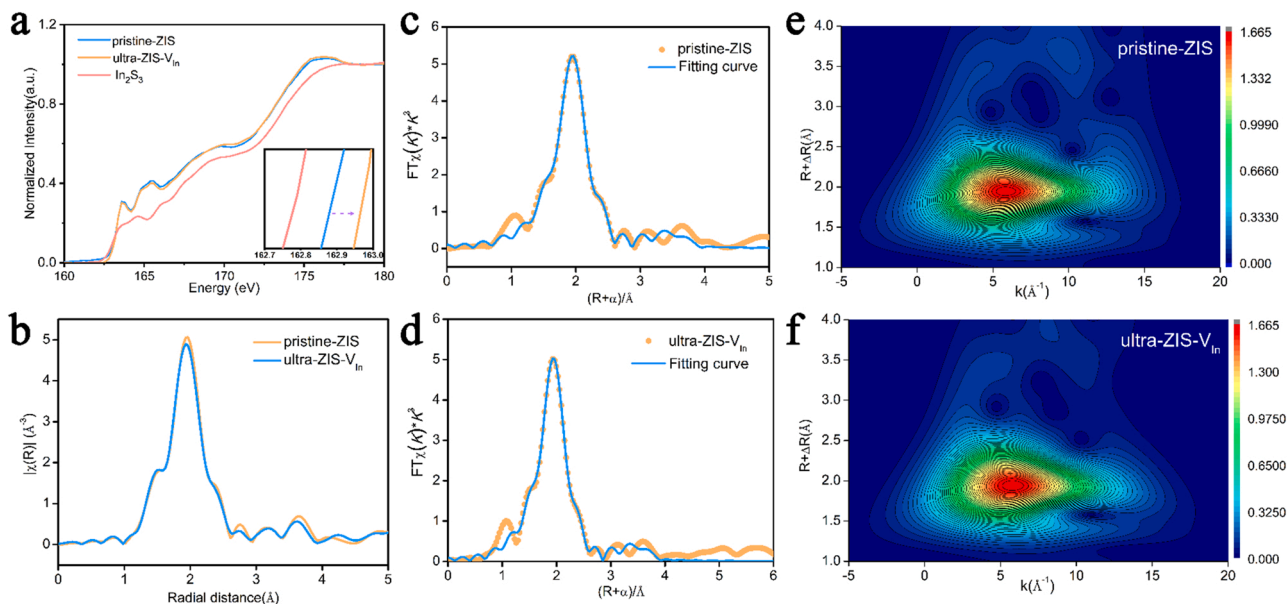


Fig. 3. Chemical states and coordination structures of pristine-ZIS and ultra-ZIS-V_{In}. (a) The normalized S L-edge XANES spectra, (b) Fourier transforms of In K-edge k^3 -weighted EXAFS spectra in R space, (c–d) the EXAFS fitting curves in R space of pristine-ZIS and ultra-ZIS-V_{In}, and (e–f) wavelet transform (WT) contour plots of pristine-ZIS and ultra-ZIS-V_{In}.

the central-peripheral. For each path, the structural parameters, like coordination number (N), interatomic distance (R), and edge-energy shift (ΔE_0) are opened to be varied.

2.4. Computational details

To describe the electronic structure of prepared materials accurately, the periodic DFT simulations were performed by employing the

Cambridge Sequential Total Energy Package (CASTEP) within Materials Studio software [28–30]. From the perspective of reality, a slab containing a 14-atom layer of materials and a 15 Å vacuum is modeled. During the optimization of structures, both atomic positions and the cell were fully relaxed. The convergence criterion for force, energy, stress and displacement were set to 5.0×10^{-6} eV/atom, 0.01 eV/Å, 0.02 GPa and 5.0×10^{-4} Å, respectively. The geometry optimization and electronic state calculation were conducted using Perdew-Burke-Ernzerhof

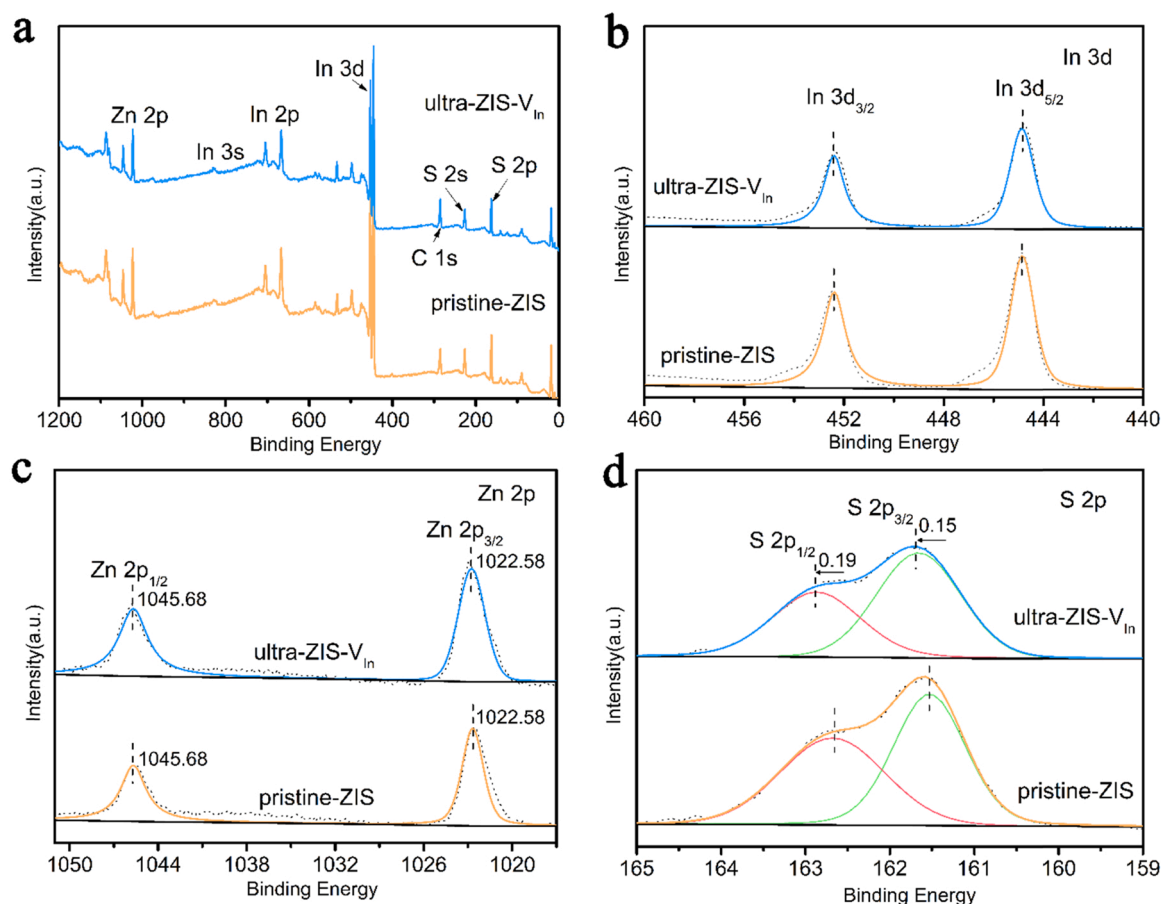


Fig. 4. (a) XPS spectra for a survey scan and high-resolution XPS spectra of (b) In 3d, (c) Zn 2p, (d) S 2p in pristine-ZIS and ultra-ZIS-V_{In}.

(PBE) exchange-correlation functional [31] with a plane wave cutoff energy of 500 eV. A $3 \times 3 \times 1$ k -point mesh was sampled using Monkhorst-Pack grid [32], while a 5.0×10^{-7} eV convergence criterion was chosen for electronic minimization.

2.5. Photocatalytic activity test

Typically, 5 mg of photocatalyst is dispersed in 20 mL aqueous solution containing 25 vol% TEOA as sacrificial electron donor. The photocatalytic reaction is carried out in a closed system with a volume 54 mL (34 mL for calculating H₂ evolution), and the reaction system is bubbled with argon gas through the reactor for 30 min to remove the dissolved oxygen. A 300 W Xenon lamp is used as a simulated solar light source with a UV-light cutoff filter ($\lambda \geq 420$ nm). The volume of H₂ is measured by a gas chromatograph (SHIMADZU GC-2014, TCD). Wavelength dependence of the hydrogen evolution is detected under irradiation with various band-pass filter including 365, 400, 425, 500, 550, and 600 nm.

3. Results and discussion

3.1. Optimized structure and Mulliken order analysis

The unit-cell of ZnIn₂S₄ is composed of two ZnIn₂S₄ monolayer (i.e., one half unit cell) (Fig. S1) by van der Waals (vdW) interlayer interaction. The half unit cell of ZnIn₂S₄ is composed of [ZnS]₄ tetrahedron, [InS]₄ tetrahedron and [InS]₆ octahedron. In [ZnS]₄ tetrahedron, each Zn atom connects with three S (I) and one S (II). In [InS]₄ tetrahedron, each In (II) atom coordinates with one S (III) atom and three S (IV) atoms. As to [InS]₆ octahedron, the In (I) atom bonds with three S (II)

atom and three S (III) atoms to form an octahedron [33,34]. As we know, numerical values of bond order quantitatively express the strength of atomic bonding, so the growth of ZnIn₂S₄ crystal can be revealed by the bond order of [ZnS]₄ tetrahedron, [InS]₄ tetrahedron and [InS]₆ octahedron [27,35]. From Mulliken bond population analysis (Table 1), the total bond order of In(I)-related bonds of 2.07 is related to two In(I)—S (II) bond and one In(I)—S(III) bonds (Fig. 1a), and 1.9 is related to one In(I)—S(II) bonds and two In(I)—S(III) bonds (Fig. 1b). As to Zn-related bonds, the total bond order of 2.96 is regarding two Zn—S(I) bonds (Fig. 1c). While In(II)-related bonds, 2.5, is related to two In(II)—S(IV) bonds (Fig. 1d). The bond order (B) relationship ($B_{[In-S]}$ in [InS]₆ interlayer < $B_{[In-S]}$ in [InS]₄ surface layer < $B_{[Zn-S]}$ in [ZnS]₄ surface layer) reflects the relative quantity of bond energy. As a result, the hard coordination of In(I) with S atoms leads to the sluggish formation of In(I)—S bonds during the hydrothermal reaction. Finally, ultra-ZIS-V_{In} nanosheets, containing a In defect-rich [InS]₆ interlayer and perfect [InS]₄ and [ZnS]₄ surface layers, are prepared with a rapid heating-up hydrothermal process.

3.2. Morphology and structure analysis

Three diffraction peaks of as-prepared ultra-ZIS-V_{In} nanosheets at 21.6°, 27.7°, 47.3° correspond to (006), (102), (110) facets of hexagonal ZnIn₂S₄ structure respectively (JCPDS card no. 72-0773, $a = 3.85$ Å, $c = 24.68$ Å) (Fig. 2a) [25,36]. The ultra-ZIS-V_{In} nanosheet, prepared with a heating-up rate of 5 °C/min and kept at 200 °C for 24 h, exhibits wrinkled morphology (Fig. S2a–b). The uniform thickness of ultra-ZIS-V_{In} nanosheets is about 2.4 nm (Fig. 2b), which is similar with that of one-unit-cell ZnIn₂S₄. The pristine-ZIS nanosheets, prepared with a heating-up rate of 2 °C/min and kept at 200 °C for 24 h, is about 10 nm

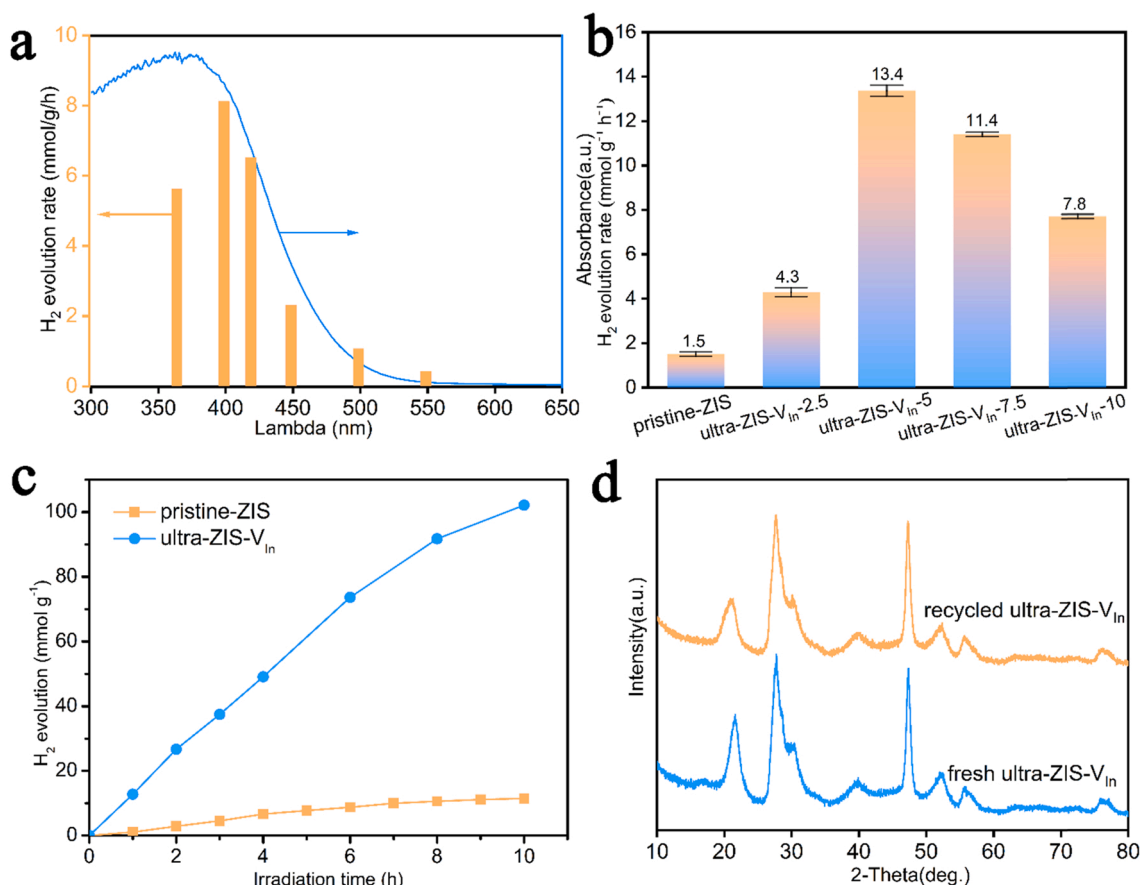


Fig. 5. (a) Wavelength dependence of the hydrogen evolution, (b) Photocatalytic hydrogen evolution reaction activities of pristine-ZIS and ultra-ZIS-V_{In} (heating rate, 2.5 °C/min, 2.5 °C/min, 5 °C/min, 7.5 °C/min, 10 °C/min), (c) Stability test for 10 h and (d) X-ray diffraction pattern for fresh ultra-ZIS-V_{In} and recycled ultra-ZIS-V_{In}.

in thickness (Fig. S2c–d). The existence of In defects in ultra-ZIS-V_{In} nanosheets can be collaboratively proved by electron paramagnetic resonance (EPR) and inductively coupled plasma optical emission spectrometer (ICP-OES). Briefly, the single-electron signal of unbonded electrons (Fig. 2c) confirms the presence of defects in ultra-ZIS-V_{In} nanosheets. The distinct signal located at 351 mT (g-value of 2.003) corresponds to the electrons captured by the In vacancies [37,38]. Furthermore, quantitative analysis of elements shows that the atomic ratio of Zn, In and S of ultra-ZIS-V_{In} nanosheets is 1:1.82:3.83 and that of pristine-ZIS nanosheets is 1:2.01:3.85 (Table S1). The molar ratios of Zn and S elements are close to the stoichiometric 1:4 in both samples, while the percentage of In elements in ultra-ZIS-V_{In} is significantly reduced compared to that in pristine-ZIS, which indicates the existence of In deficiency in ultra-ZIS-V_{In}. High angle annular dark field image scanning transmission electron microscope (HAADF-STEM) technique is employed to investigate the distribution of In defects (Fig. 2e–f). In HAADF-STEM imaging mode, the atomic contrast is roughly proportional to Z (Z denoting the atomic number) [39]. The bright spots represent In atoms (Z = 49), forming a hexagonal ring. The weak spots denote Zn atoms (Z = 30), located at center of each hexagonal ring. Partially In atom in hexagonal ring is invisible (marked by the black circle), which means the In defects are distributed in ultra-ZIS-V_{In} nanosheets (Fig. 2e). In addition, the similar intensity profiles of the Zn atoms mean the uniform distribution of Zn atoms in ultra-ZIS-V_{In} nanosheets, while the intensity profiles of partial In atoms are clearly weakened, which indicates the existence of In defects (Fig. 2f).

The local chemical state and coordination environment of the ultra-ZIS-V_{In} nanosheets are investigated by core-level X-ray absorption fine structure spectroscopy (XAFS) technology. The In K-edge X-ray

absorption near-edge structure (XANES) spectroscopy of pristine-ZIS and ultra-ZIS-V_{In} nanosheets show similar pre-edge features, demonstrating the same valence states of In atoms (Fig. S6a). Similarly, Zn K-edge features confirm the same valence states of Zn atoms in pristine-ZIS and ultra-ZIS-V_{In} nanosheets (Fig. S6b). The valence states of In and Zn prove that almost no S defect exists in ultra-ZIS-V_{In} nanosheets. The S L-edge XANES spectroscopy demonstrates that the absorption edge of ultra-ZIS-V_{In} shifts to a higher energy level than that of pristine-ZIS, which confirms the presence of cation defects (Fig. 3a). The Fourier transformed (FT) *k*³-weighted phase uncorrected In K-edge extended X-ray absorption fine structure (EXAFS) spectra with two main peaks at 1.93 Å and 2.76 Å, correspond to the In-S and In-In scattering contribution respectively (Fig. 3b). The decreased peak intensities of ultra-ZIS-V_{In} suggest that In coordination number of ultra-ZIS-V_{In} nanosheets is lower than that of pristine-ZIS [40]. Based on the EXAFS oscillation extracted from K-edge spectra and the quantitative least squares EXAFS curve-fitting [41], the coordination numbers of the In atoms in ultra-ZIS-V_{In} nanosheets are 3.9, 5.9 and 5.5, corresponding to the scattering contribution of In-S₁ (tetra-coordination), In-S₂ (hexa-coordination), and In-In (Table S2), respectively. The decreased In-In coordination number from 5.9 to 5.5, and similar In-S₁ and In-S₂ coordination number in both samples, indicate the existence of In vacancies in ultra-ZIS-V_{In} nanosheets. EXAFS wavelet transform (WT) analysis supplies radial distance and *k* space resolution to discriminate the backscattering atoms (Fig. 3c–f) [42,43]. In-S scattering paths and the In-In scattering paths are centered at (1.96 Å, 5.52 Å⁻¹) and (3.47 Å, 4.28 Å⁻¹) respectively. The similar In-S scattering paths at (1.96 Å, 5.52 Å⁻¹) confirm the same S-atom distribution at the first-shell of In atoms in pristine-ZIS and ultra-ZIS-V_{In} nanosheets, which indicates no S vacancies in ultra-ZIS-V_{In}

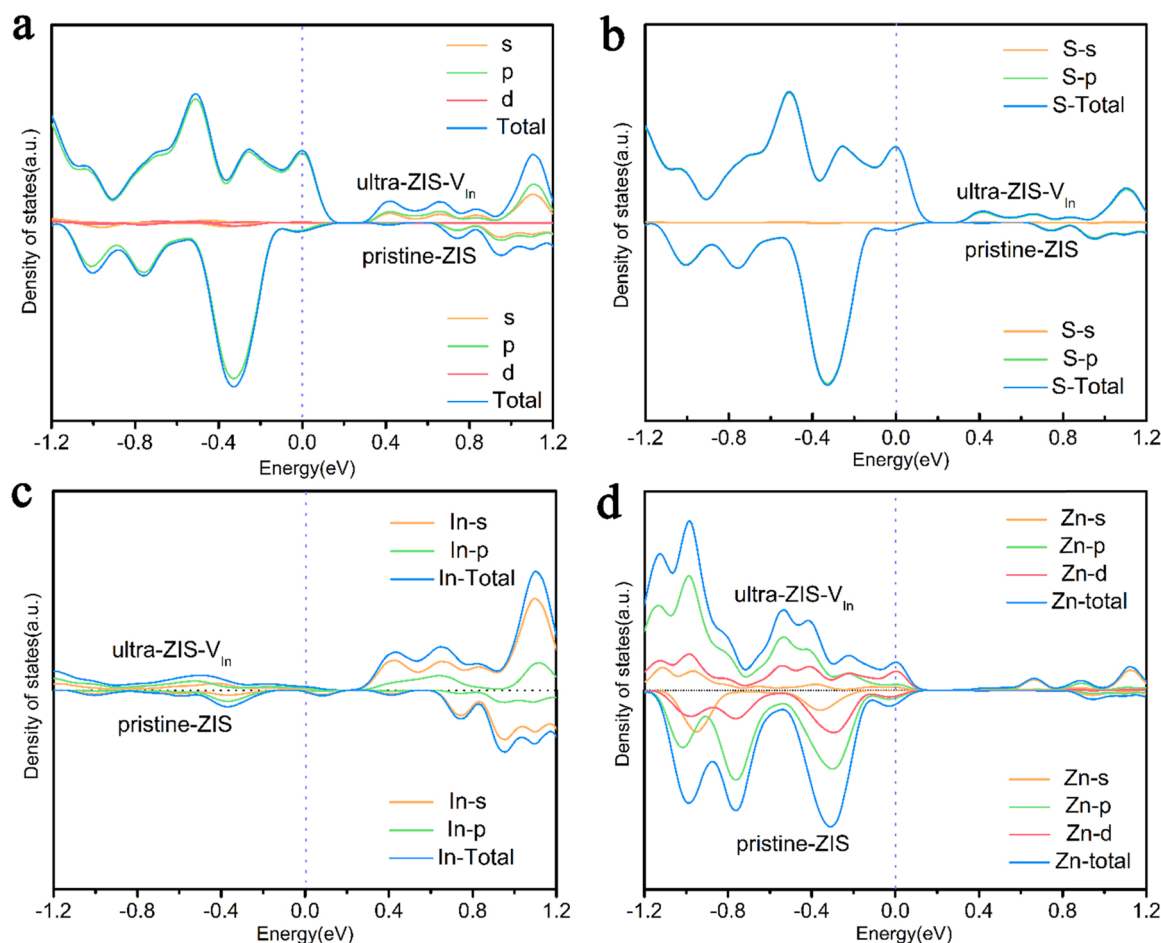


Fig. 6. The partial density of states of (a) total orbital, (b) S atomic orbital, (c) In atomic orbital, (d) Zn atomic orbital for pristine-ZIS structural model and ultra-ZIS- V_{In} structure. (The states at VBM and CBM originate mainly from S-3p orbital, for pristine-ZIS. However, the ultra-ZIS- V_{In} exhibits immensely different electronic structure from the pristine-ZIS attributing to the introduction of In vacancies. The VBM contributed mainly by S-3p orbital, while the CBM consists In-5s orbital and In-5p orbital.).

nanosheets. While the decreased In-In scattering path at (3.47 \AA , 4.28 \AA^{-1}) proves the presence of In vacancies in ultra-ZIS- V_{In} nanosheets. In summary, the synergistical XAFS analysis of Zn and In proves the presence of In vacancies in ultra-ZIS- V_{In} .

The elemental chemical states and surface electronic condition of pristine-ZIS and ultra-ZIS- V_{In} nanosheets are revealed by X-ray photoelectron spectroscopy (XPS) [8,23]. Full scan spectra of pristine-ZIS and ultra-ZIS- V_{In} show obvious signals of Zn, In and S elements (Fig. 4a) [44, 45]. For pristine-ZIS and ultra-ZIS- V_{In} nanosheets, two characteristics peaks at 444.78 eV (In $3d_{5/2}$) and 452.37 eV (In $3d_{3/2}$) are assigned to In^{3+} valence state (Fig. 4b) [44]. The Zn $2p$ binding energy at 1022.58 eV for Zn $2p_{3/2}$ and 1045.68 eV for Zn $2p_{1/2}$ are assigned to the Zn^{2+} valence state (Fig. 4c) [15]. Noteworthy, In the -Zn-S-In- stacking structure, Zn atom, separated by S atom, is far away from the trace In defect (1.4 w\%), so the effect of In defect on Zn $3d$ binding energy shifting is negligible. The position of Zn or In characteristic peaks indicates Zn^{2+} and In^{3+} valence, which further confirms the absence of S vacancies [46,47]. However, S $2p_{3/2}$ and S $2p_{1/2}$ binding energy of ultra-ZIS- V_{In} are shift to high energy 161.65 eV and 162.85 eV , respectively (the binding energy of pristine-ZIS is located at 161.5 eV and 162.66 eV) (Fig. 4d) [46]. Also, the S L-edge XANES spectroscopy demonstrate the absorption edge of ultra-ZIS- V_{In} positive-shift from 162.95 eV of pristine-ZIS to 162.85 eV ns of ultra-ZIS- V_{In} . The increased binding energy of S $2p$ further proves the presence of In vacancies in ultra-ZIS- V_{In} nanosheets.

3.3. Photocatalytic activity analysis

The photocatalytic H_2 production activity of the pristine-ZIS and ultra-ZIS- V_{In} nanosheets are evaluated under visible light irradiation ($\lambda > 420 \text{ nm}$) with TEOA as hole scavenger [24]. The linear relationship between the evolution of hydrogen and the light absorption confirms that the evolution of hydrogen is a light-driven catalytic reaction (Fig. 5a). As we know, the vacancies efficiently separate photogenerated electron-hole pairs, and then enhance the photocatalytic activity. Controlling the heating-rate during the hydrothermal process can optimize the densities of In defects, marked as ultra-ZIS- V_{In} (heating rate, $2.5 \text{ }^\circ\text{C/min}$, $2.5 \text{ }^\circ\text{C/min}$, $5 \text{ }^\circ\text{C/min}$, $7.5 \text{ }^\circ\text{C/min}$, $10 \text{ }^\circ\text{C/min}$). In $ZnIn_2S_4$ crystal, the bond orders related to the coordinated growth of metal ions show the following relationship: the sum of two Zn—S(I) bond orders (2.96) in $[ZnS]_4$ surface layer $>$ the sum of two In(II)—S(IV) bond orders (2.5) in $[InS]_4$ surface layer $>$ the sum of one In(I)—S(II) and two In(I)—S(III) bond orders (1.9) (or two In(I)—S(II) and one In(I)—S(III) bond orders (2.07)) in the In-S interlayer. The bond order difference indicates the higher coordination ability of the Zn atoms in the $[ZnS]_4$ surface layer and In atoms in the $[InS]_4$ surface layer is stronger than that of In atoms in the $[InS]_6$ interlayer. Therefore, the growth rates of $[InS]_4$ surface layer and $[ZnS]_4$ surface layer are faster than that of $[InS]_6$ interlayer. In the slow heating process, all atoms can participate in the coordination, giving rise to a perfect $ZnIn_2S_4$ crystal. While the rapid heating-up process, the weak coordination ability and insufficient coordination chance of In atoms result in the In defects in $[InS]_6$ interlayer.

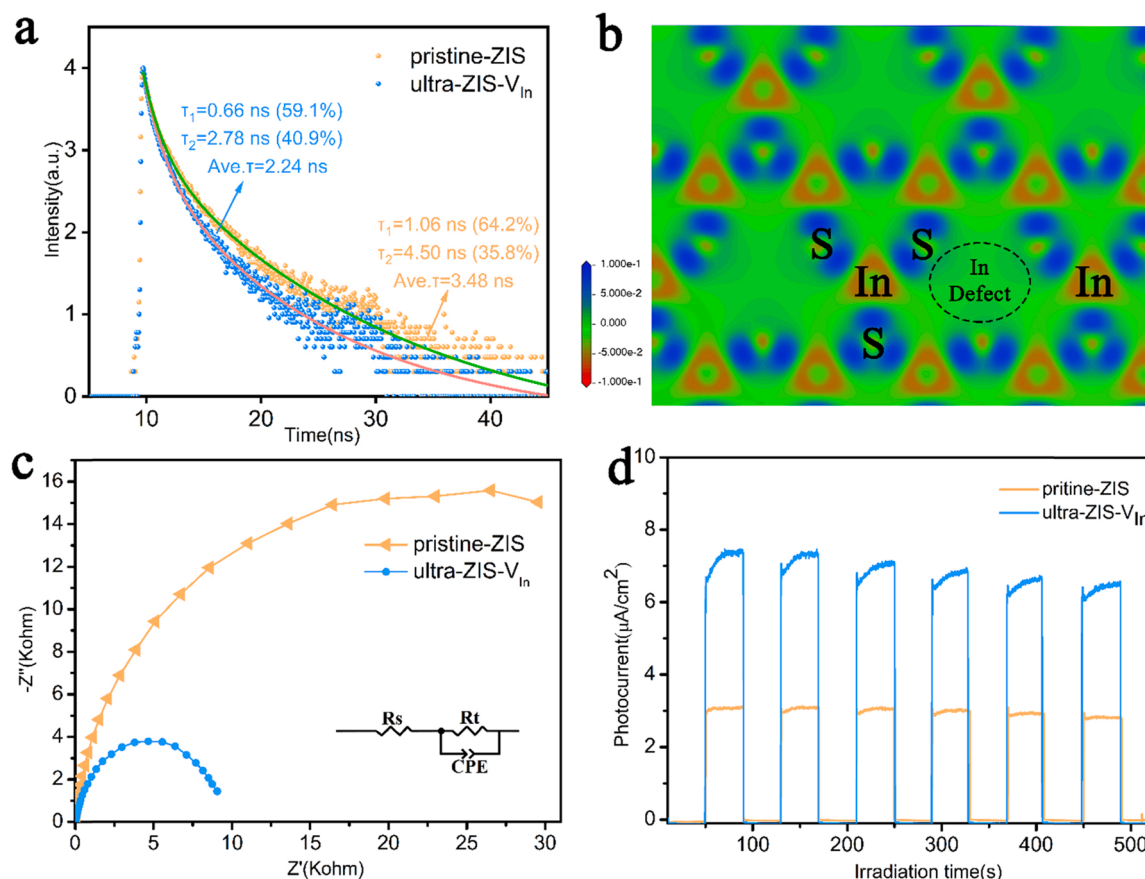


Fig. 7. (a) TRPL decay spectra of pristine-ZIS and ultra-ZIS-V_{In}, (b) Electron difference density of ultra-ZIS-V_{In}, (c) EIS Nyquist plots and (d) transient photocurrent responses of pristine-ZIS and ultra-ZIS-V_{In}.

Further, the heating rate in the hydrothermal reaction regulates the proportion of In defects. Previous reports confirm that appropriate vacancies enhance the photocatalytic activity, while excessive vacancies, acting as combination centers of photogenerated carriers, inhibits photocatalytic activity [8,48]. The heating-up rate significantly influences the photocatalytic activity, and the maximum hydrogen evolution rate reaches up to $13.4 \text{ mmol h}^{-1} \text{ g}^{-1}$ for ultra-ZIS-V_{In}-5 (Fig. 5b), 8.9 times higher than that of pristine-ZIS ($1.5 \text{ mmol h}^{-1} \text{ g}^{-1}$). The activity is even higher than that of ZIS-based photocatalysts (Table S3). Further, totally H₂ yield of ultra-ZIS-V_{In} is 0.51 mmol over 10 h and H₂ evolution rate reaches up to $10.2 \text{ mmol h}^{-1} \text{ g}^{-1}$, which linearly increases within irradiation time. While totally H₂ yield of pristine-ZIS is only 0.057 mmol over 10 h and H₂ evolution rate is only $1.1 \text{ mmol h}^{-1} \text{ g}^{-1}$ (Fig. 5c). Furthermore, the ultra-ZIS-V_{In} with excellent photocatalytic activity exhibits remarkable stability. After a 10-h illumination, ultra-ZIS-V_{In} still maintains a high photocatalytic activity, and the crystal structure (Fig. 5d) and morphology (Fig. S9a) of recycled ultra-ZIS-V_{In} are similar as those of fresh ones. Moreover, EPR and XPS results also confirm that the In-defects are stable in the ultra-ZIS-V_{In} nanosheets even after 10 h reaction (Fig S9b–f).

3.4. Density of states analysis

DFT calculation is employed to investigate the orbital distribution near the edge of valence band. The In vacancies reduce the distance between the surface Zn-S layer and the In-S octahedral layer, while increase the distance between the intermediate Zn-S layer and the In-S octahedral layer (Fig. S10a–b). Due to the distortion of the ultra-ZIS-V_{In}, the energy of the highest occupied state of S atoms in the surface [ZnS]₄ tetrahedron is higher than that of S atoms in the interlayer [ZnS]₄

tetrahedron (Fig. S10c–d). Thus, the VBM shifts from interlayer [ZnS]₄ tetrahedron to surface [ZnS]₄ tetrahedron, achieving the redistribution of the orbitals near the valence band maximum.

The DOS calculated by density functional theory (DFT), further revealed the effect of interlayer In vacancies on electronic structure and optical properties of ultra-ZIS-V_{In} nanosheets. The DOS evidences that the In defects do not affect the band gap of ultra-ZIS-V_{In} nanosheets, which are in accordance with the UV-vis results (Fig. 6a, S11a–b). However, the increased DOS of S 3p orbitals near the CBM enhances the electron-acceptance capacity of CBM (Fig. 6b). Similarly, the increased DOS of In 5s and In 5p orbitals near the VBM enhances the electron-donation capacity of VBM (Fig. 6c). Moreover, the charge carrier density (N_d) calculated by Mott-Schottky measurement increases from pristine-ZIS ($N_d = 4.03 \times 10^{21} \text{ cm}^{-3}$) to ultra-ZIS-V_{In} ($N_d = 4.52 \times 10^{21} \text{ cm}^{-3}$) (Fig S11c), consistent with the DOS calculation result. It indicates that In defects increase the carrier concentration of ultra-ZIS-V_{In} nanosheets. Overall, the enhanced electron-acceptance/donation capacity of CBM/VBM increases the concentration of carriers and improves the photocatalytic performance.

3.5. Photoelectrochemical analysis

The obvious photoluminescence (PL) emission intensity of pristine-ZIS indicates serious recombination of electron-hole pairs, which inhibits the photocatalytic activity (Fig. S13). The PL peak intensity of ultra-ZIS-V_{In} is significantly decreased, indicating that In defect effectively retards the recombination of photogenerated carriers [49,50]. Meanwhile, due to the faster separation and migration process of carriers [51,52], the radiation lifetime is shortened from 3.48 ns of pristine-ZIS to 2.24 ns of ultra-ZIS-V_{In} (Fig. 7a). Further, the TA

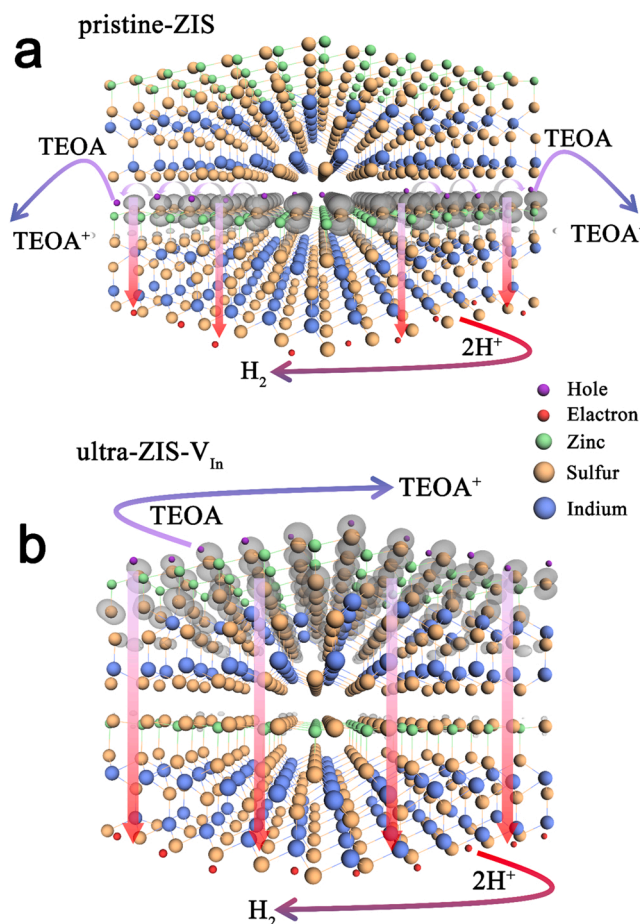


Fig. 8. The scheme for the photocatalytic hydrogen evolution (a) pristine-ZIS and (b) ultra-ZIS-V_{In}.

spectroscopy, performed under 400 nm excitation, is applied to probe the dynamics of photogenerated charge carriers. The excited state absorption (ESA) signals (625 nm) in pristine-ZIS and ultra-ZIS-V_{In} suggest that the excited electrons transition to higher excited states. In addition, the intensity of the absorption of ultra-ZIS-V_{In} is stronger than that of pristine-ZIS, indicating that more carriers are generated in ultra-ZIS-V_{In} under excitation (Fig. S14a–b). Moreover, TA decay profiles of the two samples probed at 625 nm obey the mono-exponential function. Compared the decay lifetimes of ultra-ZIS-V_{In} ($\tau = 0.97$ ps) with that of pristine-ZIS ($\tau = 0.35$ ps), the long-lived photoinduced electrons from the ultra-ZIS-V_{In} suggest the strong suppression of photoinduced charge-carriers recombination process (Fig. S14c–d). It means that In defects in ultra-ZIS-V_{In} efficiently suppress radiative recombination of carriers, and increase the quantity of the excited state electrons to participate in the reaction [53–55]. Meanwhile, the calculated work function of pristine-ZIS (001) plane and ultra-ZIS-V_{In} (001) plane are 4.65 eV and 4.09 eV versus vacuum level (Fig. S15a–b). The In vacancy reduces the work function of the In-S surface (the location of conduction band), which facilitates electrons escaping from the surface to participate in evolution [56]. The charge density of ultra-ZIS-V_{In} reveals the enhanced delocalization of electrons, indicating that In vacancies can improve the conductivity (Fig. 7b) [57]. Whilst, EIS circular diameter of ultra-ZIS-V_{In} (9.5 K Ω) is smaller than that of pristine-ZIS (32 K Ω) (Fig. 7c), indicating that In defects reduce interfacial charge-transfer resistance to improve electron transfer in ultra-ZIS-V_{In} (Fig. S16) [20, 58]. Meanwhile, the photocurrent density of ultra-ZIS-V_{In} is obviously greater than that of pristine-ZIS, revealing the efficient separation and transportation of photoinduced charge carriers in ultra-ZIS-V_{In} (Fig. 7d) [57,59]. Overall, the In defects efficiently promote the generation,

separation and migration of photogenerated carriers, and finally enhance the photocatalytic performance.

3.6. Photocatalytic reaction mechanism

DFT calculation is employed to investigate the orbital distribution near the edge of valence band, which sheds light on the essence of improved photocatalytic efficiency by In vacancies. For pristine-ZIS, the S 3p orbitals near the edge of valence band mainly localizes on the interlayer [ZnS]₄ tetrahedron (Fig. S17a). Under light irradiation, electrons transfer to the surface [InS]₄ tetrahedron from interlayer [ZnS]₄ tetrahedron, while the holes are still generated in the interlayer [ZnS]₄ tetrahedron (Fig. 8a). Due to the steric hindrance, holes hardly participate in the photocatalytic reaction. However, for ultra-ZIS-V_{In} nanosheets, In defects disturb the original periodic potential field of layered ZnIn₂S₄ crystal, and redistributed the S 3p orbitals near the edge of valence band. As a result, the S 3p orbitals near the edge of valence band transfer from the interlayer [ZnS]₄ tetrahedron to the surface [ZnS]₄ tetrahedron (Fig. S17b). Photogenerated electrons are excited to the surface [InS]₄ tetrahedron and holes are generated on the surface [ZnS]₄ tetrahedron (Fig. 8b), promoting the effective separation of photogenerated electron-hole pairs efficiently. In the photocatalytic reaction, the H⁺ is reduced to H₂ (H⁺ + e⁻ → H₂) on [InS]₄ tetrahedron surface layer. Meanwhile, TEOA are oxidized to TEOA⁺ (TEOA + h⁺ → TEOA⁺) on [ZnS]₄ surface layer tetrahedron surface layer [25]. Overall, the In defects simultaneously induce the oxidation and reduction sites to distributed on two opposite surface of layered ultra-ZIS-V_{In} nanosheets, that is [ZnS]₄ tetrahedron surface layer and [InS]₄ tetrahedron surface layer respectively.

In order to illustrate the fact that photo-generated electrons and holes of ultra-ZIS-V_{In} nanosheets distributes on [ZnS]₄ tetrahedron surface and [InS]₄ tetrahedron surface respectively, photo-deposition experiments of Ag on tetrahedron [ZnS]₄ surface and Co₃O₄ on tetrahedron [InS]₄ surface of ultra-ZIS-V_{In} nanosheets are conducted. Ag⁺ can be exclusively reduced to Ag cluster on the tetrahedron [ZnS]₄ surface where electrons are accumulated, while the Co²⁺ can be oxidized to Co₃O₄ on the tetrahedron [InS]₄ surface only where the holes are accumulated. High-resolution transmission electron microscope (HRTEM) result of Ag-deposited ultra-ZIS-V_{In} nanosheets clearly shows that the accumulation of Ag particles on one surface of the ultra-ZIS-V_{In} leads to a rough surface (Fig. S18a), while the other surface is relatively smooth (Fig. S18b). Similar phenomenon also occurs on the Co₃O₄-deposited ultra-ZIS-V_{In} nanosheets, which means the Co₃O₄ nanoparticles are exclusively deposited on the one surface of ultra-ZIS-V_{In} nanosheets. (Fig. S19c–d). Overall, the light deposition experiment further verifies the facts that electrons and holes distribute on two opposite surface of layered ultra-ZIS-V_{In} nanosheets, consistent well with the orbital distribution results calculated by DFT.

4. Conclusion

In summary, the ultra-ZIS-V_{In}, containing controllable interlayer In defect, is successfully synthesized by a rapid heating-up rate hydrothermal reaction. The interlayer In vacancies separate photogenerated electrons and holes to the opposite surface of the ultra-ZIS-V_{In} nanosheets, respectively. The holes, locating on the [ZnS]₄ surface of ultra-ZIS-V_{In}, reduce the recombination of electron-hole pairs. Moreover, the In vacancies enhance the electron-donation capacity of VBM and electron-acceptance capacity of CBM, increasing density of photo-generated carriers. Furthermore, In vacancies prompt electron delocalization, which benefits interlayer charge transport and improves the conductivity of ultra-ZIS-V_{In} nanosheets. The rapid heating-up hydrothermal method provides a significant inspiration for defect engineering in layered photocatalyst, which supplies a rational strategy for directional separation of electron-hole pairs.

CRediT authorship contribution statement

Wenjun Dong designed the light-facilitated structure reconstruction on self-optimized photocatalyst, and revised the paper. Qingjie Luan conducted structure design, experiments, characterization, analysis, and paper writing. Xiangdong Xue performed structure design and theoretical calculation. Rongjie Li and Lin Gu performed experimental characterization and analysis. Dongxue Zhou, Xing Wang and Baozhen Li performed experiments and analysis. Ge Wang and Changmin Hou revised the paper. All authors contributed to the interpretation of the results and improvement of the paper.

Declaration of Competing Interest

The authors declare that they have no known competing financial interests or personal relationships that could have appeared to influence the work reported in this paper.

Acknowledgements

This work was supported by the National Natural Science Foundation of China (52071027, 51872025), Capital's Funds for Health Improvement and Research (2021-1G-4291), the National Key Research and Development Program of China (2021YFB3802203), Beijing Natural Science Foundation (2212038), the National Defense Basic Scientific Research (JCKY2019110C036), Scientific and Technological Innovation Foundation of Foshan (BK21BE008) for financial support. The computing work is supported by USTB MatCom of Beijing Advanced Innovation Center for Materials Genome Engineering.

Appendix A. Supporting information

Supplementary data associated with this article can be found in the online version at [doi:10.1016/j.apcatb.2021.121007](https://doi.org/10.1016/j.apcatb.2021.121007).

References

- [1] G. Zhou, Y. Shan, Y. Hu, X. Xu, L. Long, J. Zhang, J. Dai, J. Guo, J. Shen, S. Li, L. Liu, X. Wu, Half-metallic carbon nitride nanosheets with micro grid mode resonance structure for efficient photocatalytic hydrogen evolution, *Nat. Commun.* 9 (2018) 3366, <https://doi.org/10.1038/s41467-018-05590-x>.
- [2] M.R. Gao, J.X. Liang, Y.R. Zheng, Y.F. Xu, J. Jiang, Q. Gao, J. Li, S.H. Yu, An efficient molybdenum disulfide/cobalt diselenide hybrid catalyst for electrochemical hydrogen generation, *Nat. Commun.* 6 (2015) 5982, <https://doi.org/10.1038/ncomms6982>.
- [3] X.Y. Liu, H. Chen, R. Wang, Y. Shang, Q. Zhang, W. Li, G. Zhang, J. Su, C.T. Dinh, F. P.G. de Arquer, J. Li, J. Jiang, Q. Mi, R. Si, X. Li, Y. Sun, Y.T. Long, H. Tian, E. H. Sargent, Z. Ning, 0D–2D quantum dot: metal dichalcogenide nanocomposite photocatalyst achieves efficient hydrogen generation, *Adv. Mater.* 29 (2017), 1605646, <https://doi.org/10.1002/adma.201605646>.
- [4] Z. Li, X. Wang, W. Tian, A. Meng, L. Yang, CoNi bimetal cocatalyst modifying a hierarchical ZnIn₂S₄ nanosheet-based microsphere noble-metal-free photocatalyst for efficient visible-light-driven photocatalytic hydrogen production, *ACS Sustain. Chem. Eng.* 7 (2019) 20190–20201, <https://doi.org/10.1021/acssuschemeng.9b06430>.
- [5] X.Y. Yu, Y. Feng, Y. Jeon, B. Guan, X.W. Lou, U. Paik, Formation of Ni-Co-MoS₂ nanoboxes with enhanced electrocatalytic activity for hydrogen evolution, *Adv. Mater.* 28 (2016) 9006–9011, <https://doi.org/10.1002/adma.201601188>.
- [6] Y. Yin, J. Han, Y. Zhang, X. Zhang, P. Xu, Q. Yuan, L. Samad, X. Wang, Y. Wang, Z. Zhang, P. Zhang, X. Cao, B. Song, S. Jin, Contributions of phase, sulfur vacancies, and edges to the hydrogen evolution reaction catalytic activity of porous molybdenum disulfide nanosheets, *J. Am. Chem. Soc.* 138 (2016) 7965–7972, <https://doi.org/10.1021/jacs.6b03714>.
- [7] G. Zuo, Y. Wang, W.L. Teo, A. Xie, Y. Guo, Y. Dai, W. Zhou, D. Jana, Q. Xian, W. Dong, Y. Zhao, Ultrathin ZnIn₂S₄ nanosheets anchored on Ti₃C₂ Tx MXene for photocatalytic H₂ evolution, *Angew. Chem. Int. Ed.* 59 (2020) 11287–11292, <https://doi.org/10.1002/anie.202002136>.
- [8] C. Du, Q. Zhang, Z. Lin, B. Yan, C. Xia, G. Yang, Half-unit-cell ZnIn₂S₄ monolayer with sulfur vacancies for photocatalytic hydrogen evolution, *Appl. Catal. B-Environ.* 248 (2019) 193–201, <https://doi.org/10.1016/j.apcatb.2019.02.027>.
- [9] X. Shi, L. Mao, P. Yang, H. Zheng, M. Fujitsuka, J. Zhang, T. Majima, Ultrathin ZnIn₂S₄ nanosheets with active (110) facet exposure and efficient charge separation for cocatalyst free photocatalytic hydrogen evolution, *Appl. Catal. B-Environ.* 265 (2020), 118616, <https://doi.org/10.1016/j.apcatb.2020.118616>.
- [10] W. Yang, L. Zhang, J. Xie, X. Zhang, Q. Liu, T. Yao, S. Wei, Q. Zhang, Y. Xie, Enhanced photoexcited carrier separation in oxygen-doped ZnIn₂S₄ nanosheets for hydrogen evolution, *Angew. Chem. Int. Ed.* 55 (2016) 6716–6720, <https://doi.org/10.1002/anie.201602543>.
- [11] M. Liu, Y. Chen, J. Su, J. Shi, X. Wang, L. Guo, Photocatalytic hydrogen production using twinned nanocrystals and an unanchored NiS_x co-catalyst, *Nat. Energy* 1 (2016) 16151, <https://doi.org/10.1038/nenergy.2016.151>.
- [12] J. Li, Z. Zhang, W. Cui, H. Wang, W. Cen, G. Johnson, G. Jiang, S. Zhang, F. Dong, The spatially oriented charge flow and photocatalysis mechanism on internal van der Waals heterostructures enhanced g-C₃N₄, *ACS Catal.* 8 (2018) 8376–8385, <https://doi.org/10.1021/acscatal.8b02459>.
- [13] W. Zhao, D. Zhai, C. Liu, D. Zheng, H. Wu, L. Sun, Z. Li, T. Yu, W. Zhou, F. Xu, S. Zhai, K. Han, Z. He, W. Deng, Unblocked intramolecular charge transfer for enhanced CO₂ photoreduction enabled by an imidazolium-based ionic conjugated microporous polymer, *Appl. Catal. B-Environ.* 300 (2021), 120719, <https://doi.org/10.1016/j.apcatb.2021.120719>.
- [14] Y. Shu, J. Ji, M. Zhou, S. Liang, Q. Xie, S. Li, B. Liu, J. Deng, J. Cao, S. Liu, H. Huang, Selective photocatalytic oxidation of gaseous ammonia at ppb level over Pt and F modified TiO₂, *Appl. Catal. B-Environ.* 300 (2021), 120688, <https://doi.org/10.1016/j.apcatb.2021.120688>.
- [15] W. Li, Z. Lin, G. Yang, A 2D self-assembled MoS₂/ZnIn₂S₄ heterostructure for efficient photocatalytic hydrogen evolution, *Nanoscale* 9 (2017) 18290–18298, <https://doi.org/10.1039/c7nr06755k>.
- [16] M. Xiong, B. Chai, J. Yan, G. Fan, G. Song, Few-layer WS₂ decorating ZnIn₂S₄ with markedly promoted charge separation and photocatalytic H₂ evolution activity, *Appl. Surf. Sci.* 514 (2020), 145965, <https://doi.org/10.1016/j.apusc.2020.145965>.
- [17] M. Ma, Z. Huang, D.E. Doronkin, W. Fa, Z. Rao, Y. Zou, R. Wang, Y. Zhong, Y. Cao, R. Zhang, Y. Zhou, Ultrahigh surface density of Co-N₂C single-atom-sites for boosting photocatalytic CO₂ reduction to methanol, *Appl. Catal. B-Environ.* 300 (2021), 120695, <https://doi.org/10.1016/j.apcatb.2021.120695>.
- [18] N. Luo, C. Chen, D. Yang, W. Hu, F. Dong, S defect-rich ultrathin 2D MoS₂: the role of S point-defects and S stripping-defects in the removal of Cr (VI) via synergistic adsorption and photocatalysis, *Appl. Catal. B-Environ.* 299 (2021), 120664, <https://doi.org/10.1016/j.apcatb.2021.120664>.
- [19] D. Fan, Y. Lu, H. Zhang, H. Xu, C. Lu, Y. Tang, X. Yang, Synergy of photocatalysis and photothermal effect in integrated 0D perovskite oxide/2D MXene heterostructures for simultaneous water purification and solar steam generation, *Appl. Catal. B-Environ.* 295 (2021), 120285, <https://doi.org/10.1016/j.apcatb.2021.120285>.
- [20] P. Wang, Z. Shen, Y. Xia, H. Wang, L. Zheng, W. Xi, S. Zhan, Atomic insights for optimum and excess doping in photocatalysis: a case study of few-layer Cu-ZnIn₂S₄, *Adv. Funct. Mater.* 29 (2019), 1807013, <https://doi.org/10.1002/adfm.201807013>.
- [21] X. Shi, L. Mao, C. Dai, P. Yang, J. Zhang, F. Dong, L. Zheng, M. Fujitsuka, H. Zheng, Inert basal plane activation of two-dimensional ZnIn₂S₄ via Ni atom doping for enhanced co-catalyst free photocatalytic hydrogen evolution, *J. Mater. Chem. A* 8 (2020) 13376–13384, <https://doi.org/10.1039/d0ta03992f>.
- [22] C. Du, B. Yan, Z. Lin, G. Yang, Enhanced carrier separation and increased electron density in 2D heavily N-doped ZnIn₂S₄ for photocatalytic hydrogen production, *J. Mater. Chem. A* 8 (2020) 207–217, <https://doi.org/10.1039/c9ta11318e>.
- [23] S. Zhang, X. Liu, C. Liu, S. Luo, L. Wang, T. Cai, Y. Zeng, J. Yuan, W. Dong, Y. Pei, Y. Liu, MoS₂ quantum dot growth induced by S vacancies in a ZnIn₂S₄ monolayer: atomic-level heterostructure for photocatalytic hydrogen production, *ACS Nano* 12 (2018) 751–758, <https://doi.org/10.1021/acsnano.7b07974>.
- [24] M.Q. Yang, Y.J. Xu, W. Lu, K. Zeng, H. Zhu, Q.H. Xu, G.W. Ho, Self-surface charge exfoliation and electrostatically coordinated 2D hetero-layered hybrids, *Nat. Commun.* 8 (2017) 14224, <https://doi.org/10.1038/ncomms14224>.
- [25] X. Jiao, Z. Chen, X. Li, Y. Sun, S. Gao, W. Yan, C. Wang, Q. Zhang, Y. Lin, Y. Luo, Y. Xie, Defect-mediated electron-hole separation in one-unit-cell ZnIn₂S₄ layers for boosted solar-driven CO₂ reduction, *J. Am. Chem. Soc.* 139 (2017) 7586–7594, <https://doi.org/10.1021/jacs.7b02290>.
- [26] X. Wang, X. Wang, J. Huang, S. Li, A. Meng, Z. Li, Interfacial chemical bond and internal electric field modulated Z-scheme S_v-ZnIn₂S₄/MoSe₂ photocatalyst for efficient hydrogen evolution, *Nat. Commun.* 12 (2021) 4112, <https://doi.org/10.1038/s41467-021-24511-z>.
- [27] K. Ding, Y. Li, B. Chen, Y. Zhang, Original investigation of a novel photocatalyst driven by visible light: ZnIn₂S₄, *J. Phys. Soc. Jpn* 83 (2014), 074301, <https://doi.org/10.7556/jpsj.83.074301>.
- [28] M.D.S. Stewart, J. Clark, Chris J. Pickard, Phil J. Hasnip, Matt I.J. Probert, Keith Refson, Mike C. Payne, First principles methods using CASTEP, *Z. Krist.* 220 (2005) 567–570, <https://doi.org/10.1524/zkri.220.5.567.65075>.
- [29] W. Kohn, L.J. Sham, Self-consistent equations including exchange and correlation effects, *Phys. Rev.* 140 (1965) A1133–A1138, <https://doi.org/10.1103/PhysRev.140.A1133>.
- [30] M.C. Payne, M.P. Teter, D.C. Allan, T.A. Arias, J.D. Joannopoulos, Iterative minimization techniques for ab initio total-energy calculations: molecular dynamics and conjugate gradients, *Rev. Mod. Phys.* 64 (1992) 1045–1097, <https://doi.org/10.1103/RevModPhys.64.1045>.
- [31] K.B. John, P. Perdew, Matthias Ernzerhof, Generalized gradient approximation made simple, *Phys. Rev. Lett.* 77 (1996) 3865–3868, <https://doi.org/10.1103/PhysRevLett.77.3865>.
- [32] H.J. Monkhorst, J.D. Pack, Special points for Brillouin-zone integrations, *Phys. Rev. B* 13 (1976) 5188–5192, <https://doi.org/10.1103/PhysRevB.13.5188>.
- [33] J. Zhao, D. Mei, Y. Yang, W. Cao, C. Liu, Y. Wu, Z. Lin, Rb₁₀Zn₄Sn₄S₁₇: a chalcogenide with large laser damage threshold improved from the Mn-based

- analogue, *Inorg. Chem.* 58 (2019) 15029–15033, <https://doi.org/10.1021/acs.inorgchem.9b02481>.
- [34] C. Liu, D. Mei, W. Cao, Y. Yang, Y. Wu, G. Li, Z. Lin, Mn-based tin sulfide $\text{Sr}_3\text{MnSn}_2\text{S}_8$ with a wide band gap and strong nonlinear optical response, *J. Mater. Chem. C* 7 (2019) 1146–1150, <https://doi.org/10.1039/c8tc05904g>.
- [35] L.R.Z.K. Chen, Electronic character of interdiffusion of metals in nickel, *J. Mater. Sci.* 40 (2005) 2569–2571, <https://doi.org/10.1007/s10853-005-2075-8>.
- [36] G. Wang, G. Chen, Y. Yu, X. Zhou, Y. Teng, Mixed solvothermal synthesis of hierarchical ZnIn_2S_4 spheres: specific facet-induced photocatalytic activity enhancement and a DFT elucidation, *RSC Adv.* 3 (2013) 18579–18586, <https://doi.org/10.1039/c3ra42245c>.
- [37] S. Meng, C. C. X. G. H. W. Q. M. J. Z. S. C. X. F. D. L., W. L., Efficient photocatalytic H_2 evolution, CO_2 reduction and N_2 fixation coupled with organic synthesis by cocatalyst and vacancies engineering, *Appl. Catal. B-Environ.* 285 (2021) 11978, <https://doi.org/10.1016/j.apcatb.2020.119789>.
- [38] X. Gong, L. Tang, J. Zou, Z. Guo, Y. Li, L. Jia, H. Liu, M. Liu, L. Zhou, P. Huang, H. Ruan, Y. Lu, W. Zhu, R. He, Introduction of cation vacancies and iron doping into TiO_2 enabling efficient uranium photoreduction, *J. Hazard. Mater.* 423 (2022), 126935, <https://doi.org/10.1016/j.jhazmat.2021.126935>.
- [39] Z. Wang, M. Saito, K.P. McKenna, L. Gu, S. Tsukimoto, A.L. Shluger, Y. Ikumura, Atom-resolved imaging of ordered defect superstructures at individual grain boundaries, *Nature* 479 (2011) 380–383, <https://doi.org/10.1038/nature10593>.
- [40] J. Hu, L. Yu, J. Deng, Y. Wang, K. Cheng, C. Ma, Q. Zhang, W. Wen, S. Yu, Y. Pan, J. Yang, H. Ma, F. Qi, Y. Wang, Y. Zheng, M. Chen, R. Huang, S. Zhang, Z. Zhao, J. Mao, X. Meng, Q. Ji, G. Hou, X. Han, X. Bao, Y. Wang, D. Deng, Sulfur vacancy-rich MoS_2 as a catalyst for the hydrogenation of CO_2 to methanol, *Nat. Catal.* 4 (2021) 242–250, <https://doi.org/10.1038/s41929-021-00584-3>.
- [41] J. Wang, Y. Zhao, G. Li, D. Luo, J. Liu, Y. Zhang, X. Wang, L. Shui, Z. Chen, Aligned sulfur-deficient ZnS_{1-x} nanotube arrays as efficient catalyzer for high-performance lithium/sulfur batteries, *Nano Energy* 84 (2021), 105891, <https://doi.org/10.1016/j.nanoen.2021.105891>.
- [42] S. Deng, M. Luo, C. Ai, Y. Zhang, B. Liu, L. Huang, Z. Jiang, Q. Zhang, L. Gu, S. Lin, X. Wang, L. Yu, J. Wen, J. Wang, G. Pan, X. Xia, J. Tu, Synergistic doping and intercalation: realizing deep phase modulation on MoS_2 arrays for high-efficiency hydrogen evolution reaction, *Angew. Chem. Int. Ed.* 58 (2019) 16289–16296, <https://doi.org/10.1002/anie.201909698>.
- [43] Y. Zang, S. Niu, Y. Wu, X. Zheng, J. Cai, J. Ye, Y. Xie, Y. Liu, J. Zhou, J. Zhu, X. Liu, G. Wang, Y. Qian, Tuning orbital orientation endows molybdenum disulfide with exceptional alkaline hydrogen evolution capability, *Nat. Commun.* 10 (2019) 1217, <https://doi.org/10.1038/s41467-019-09210-0>.
- [44] Q. Liu, H. Lu, Z. Shi, F. Wu, J. Guo, K. Deng, L. Li, 2D ZnIn_2S_4 nanosheet/1D TiO_2 nanorod heterostructure arrays for improved photoelectrochemical water splitting, *ACS Appl. Mater. Interfaces* 6 (2014) 17200–17207, <https://doi.org/10.1021/am505015j>.
- [45] S. Peng, P. Zhu, V. Thavasi, S.G. Mhaisalkar, S. Ramakrishna, Facile solution deposition of ZnIn_2S_4 nanosheet films on FTO substrates for photoelectric application, *Nanoscale* 3 (2011) 2602–2608, <https://doi.org/10.1039/c0nr00955e>.
- [46] X. Zhang, Z. Zhao, W. Zhang, G. Zhang, D. Qu, X. Miao, S. Sun, Z. Sun, Surface defects enhanced visible light photocatalytic H_2 production for Zn-Cd-S solid solution, *Small* 12 (2016) 793–801, <https://doi.org/10.1002/smll.201503067>.
- [47] Y. He, H. Rao, K. Song, J. Li, Y. Yu, Y. Lou, C. Li, Y. Han, Z. Shi, S. Feng, 3D hierarchical ZnIn_2S_4 nanosheets with rich Zn vacancies boosting photocatalytic CO_2 reduction, *Adv. Funct. Mater.* 29 (2019), 1905153, <https://doi.org/10.1002/adfm.201905153>.
- [48] Z. Yi, N.H. Ladi, X. Shai, H. Li, Y. Shen, M. Wang, Will organic-inorganic hybrid halide lead perovskites be eliminated from optoelectronic applications? *Nanoscale Adv.* 1 (2019) 1276–1289, <https://doi.org/10.1039/c8na00416a>.
- [49] H. Zhang, P. Zhang, M. Qiu, J. Dong, Y. Zhang, X.W.D. Lou, Ultrasmall MoO_x clusters as a novel cocatalyst for photocatalytic hydrogen evolution, *Adv. Mater.* 31 (2019), 1804883, <https://doi.org/10.1002/adma.201804883>.
- [50] X. Li, S. Fang, L. Ge, C. Han, P. Qiu, W. Liu, Synthesis of flower-like Ag/AgCl- Bi_2MoO_6 plasmonic photocatalysts with enhanced visible-light photocatalytic performance, *Appl. Catal. B-Environ.* 176 (2015) 62–69, <https://doi.org/10.1016/j.apcatb.2015.03.042>.
- [51] H. Wang, X. Sun, D. Li, X. Zhang, S. Chen, W. Shao, Y. Tian, Y. Xie, Boosting hot-electron generation: exciton dissociation at the order-disorder interfaces in polymeric photocatalysts, *J. Am. Chem. Soc.* 139 (2017) 2468–2473, <https://doi.org/10.1021/jacs.6b12878>.
- [52] Z. Zhang, Y. Huang, K. Liu, L. Guo, Q. Yuan, B. Dong, Multichannel-improved charge-carrier dynamics in well-designed hetero-nanostructural plasmonic photocatalysts toward highly efficient solar-to-fuels conversion, *Adv. Mater.* 27 (2015) 5906–5914, <https://doi.org/10.1002/adma.201502203>.
- [53] P. Niu, M. Qiao, Y. Li, L. Huang, T. Zhai, Distinctive defects engineering in graphitic carbon nitride for greatly extended visible light photocatalytic hydrogen evolution, *Nano Energy* 44 (2018) 73–81, <https://doi.org/10.1016/j.nanoen.2017.11.059>.
- [54] L. Zhang, W. Wang, D. Jiang, E. Gao, S. Sun, Photoreduction of CO_2 on BiOCl nanoplates with the assistance of photoinduced oxygen vacancies, *Nano Res.* 8 (2015) 821–831, <https://doi.org/10.1007/s12274-014-0564-2>.
- [55] J.Y. Bai, L.J. Wang, Y.J. Zhang, C.F. Wen, X.L. Wang, H.G. Yang, Carboxyl functionalized graphite carbon nitride for remarkably enhanced photocatalytic hydrogen evolution, *Appl. Catal. B-Environ.* 266 (2020), 118590, <https://doi.org/10.1016/j.apcatb.2020.118590>.
- [56] Z. Yang, X. Xia, W. Yang, L. Wang, Y. Liu, Photothermal effect and continuous hot electrons injection synergistically induced enhanced molecular oxygen activation for efficient selective oxidation of benzyl alcohol over plasmonic $\text{W}_{18}\text{O}_{49}/\text{ZnIn}_2\text{S}_4$ photocatalyst, *Appl. Catal. B-Environ.* 299 (2021), 120675, <https://doi.org/10.1016/j.apcatb.2021.120675>.
- [57] Y. Zhao, Y. Zhao, R. Shi, B. Wang, G.I.N. Waterhouse, L.Z. Wu, C.H. Tung, T. Zhang, Tuning oxygen vacancies in ultrathin TiO_2 nanosheets to boost photocatalytic nitrogen fixation up to 700 nm, *Adv. Mater.* 31 (2019), 1806482, <https://doi.org/10.1002/adma.201806482>.
- [58] J. Ran, J. Zhang, J. Yu, S.Z. Qiao, Enhanced visible-light photocatalytic H_2 production by $\text{Zn}_x\text{Cd}_{1-x}\text{S}$ modified with earth-abundant nickel-based cocatalysts, *ChemSusChem* 7 (2014) 3426–3434, <https://doi.org/10.1002/cssc.201402574>.
- [59] J. Lv, P. Liu, F. Yang, L. Xing, D. Wang, X. Chen, H. Gao, X. Huang, Y. Lu, G. Wang, 3D hydrangea macrophylla-like nickel-vanadium metal-organic frameworks formed by self-assembly of ultrathin 2D nanosheets for overall water splitting, *ACS Appl. Mater. Interfaces* 12 (2020) 48495–48510, <https://doi.org/10.1021/acsami.0c11722>.